AGU100 ADVANCING EARTH AND SPACE SCIENCE

JGR Space Physics

RESEARCH ARTICLE
10.1029/2018JA026278

Special Section:
Particle Dynamics in the Earth's Radiation Belts

Key Points:
- A dropout event during the 2015 St. Patrick's Day storm is examined to find the electron flux lost to the atmosphere
- Clear perturbations in VLF signal amplitude and phase are seen at $L \approx$ 3–4.5 at the time of the dropout event
- Less than ~0.5% of the relativistic flux lost at $L \approx 4$ during the dropout was due to precipitation into the atmosphere

Correspondence to:
S. Gokani,
gokanisneha@gmail.com

Citation:
Gokani, S. A., Kosch, M., Clilverd, M., Rodger, C. J., & Sinha, A. K. (2019). What Fraction of the Outer Radiation Belt Relativistic Electron Flux at L ≈ 3-4 .5 Was Lost to the Atmosphere During the Dropout Event of the St. Patrick's Day Storm of 2015? *Journal of Geophysical Research: Space Physics*, *124*, 9537–9551. https://doi.org/10.1029/2018JA026278

Received 8 NOV 2018
Accepted 24 SEP 2019
Published online 21 NOV 2019

What Fraction of the Outer Radiation Belt Relativistic Electron Flux at L ≈ 3-4.5 Was Lost to the Atmosphere During the Dropout Event of the St. Patrick's Day Storm of 2015?

Sneha A. Gokani[1,2], Mike Kosch[3,4,5], Mark Clilverd[6], Craig J. Rodger[7], and Ashwini K. Sinha[1]

[1]Geophysical Studies in Polar Regions, Indian Institute of Geomagnetism, New Panvel, Navi Mumbai, India, [2]State Key Laboratory of Marine Geology and School of Ocean and Earth Science, Tongji University, Shanghai, China, [3]South African National Space Agency, Hermanus, South Africa, [4]Department of Physics, Lancaster University, Bailrigg, Lancaster, UK, [5]Department of Physics and Astronomy, University of Western Cape, Bellville, South Africa, [6]British Antarctic Survey, Cambridge, England, [7]Department of Physics, University of Otago, Dunedin, New Zealand

Abstract Observations of relativistic energetic electron fluxes in the outer radiation belt can show dropouts, that is, sudden electron flux depletions during the main phase of a geomagnetic storm. Many recent studies show that these dropouts typically involve a true loss of particles, that is, nonadiabatic losses in nature. Precipitation into the atmosphere of relativistic electrons driven into the bounce loss cone, through wave-particle interactions, is envisaged as one of the primary loss mechanisms. Such precipitation can be studied using ground-based observations such as VLF narrowband radio waves, due to the deposition of energy into the lower ionospheric D-region, thereby modifying the subionospheric waveguide. The present study focuses on the dropout event observed during the St. Patrick's Day storm of March 2015. Perturbations lasting several hours were observed in the received VLF amplitude and phase of the NAA transmitter signal measured at Seattle and Edmonton and the NML transmitter signal received at St. John's and Edmonton. All these $L \approx$ 3–4.5 paths were located on the nightside of the Earth during dropout phase of the storm. Observations of relativistic electron characteristics from Van Allen Probes, and ionospheric perturbation characterization from VLF radio waves, are used to calculate that during the time interval of the dropout event, <0.5% of the relativistic fluxes involved in the dropout event were lost to the atmosphere. This leads to the conclusion that relativistic electron precipitation was not the major contributor to the observed dropout event at $L \approx 4$ that occurred during the St. Patrick's Day storm of March 2015.

1. Introduction

The radiation belts are formed as a consequence of trapping charged particles by Earth's magnetic field. Populated by energetic electrons and protons, these belts are distributed in two distinct toroidal zones known as "inner" and "outer" belts, separated by a slot region. The relatively stable inner belt is centered on $L \approx 1.4$ and extends up to about $L \approx 2$ with electrons having characteristic energy levels of a few tens of keV. The dynamic outer belt is centered on $L \approx 4$ and extends from $L \approx$ 3–6 with electrons having characteristic energies of 100's of keV to a few MeV. The slot region ($L \approx$ 2–2.5) is thought to be the result of energetic electron precipitation losses through wave-particle interactions (Kivelson & Russell, 1995; Lyons & Thorne, 1973). Though radiation belt physics have been studied from the beginning of the Space Era, the launch of NASA's Van Allen Probes mission gained much attention as it was dedicated to develop much deeper understanding of radiation belt structure and dynamics (Mauk et al., 2012). Since their launch in 2012, the Van Allen Probes have provided the most comprehensive in situ measurements to date.

The structure and variability of electron fluxes in the outer radiation belt are believed to be controlled by the competition between source and loss processes (Millan & Thorne, 2007), which can alter greatly during intense geomagnetic activity (Bortnik et al., 2006; Herrera et al., 2016; Turner et al., 2014; Ukhorskiy et al., 2006; Zhang et al., 2016). However, the net increase or decrease of outer belt electron flux is decided by a delicate balance between particle acceleration and loss (Reeves et al., 2003). These source, loss, and transport processes show temporal and spatial variations depending upon the complex plasma conditions that are driven by the solar wind and the interplanetary magnetic field. The radiation belt source process is often manifested by the acceleration of electrons in the outer belt. This acceleration can sometimes be provided by inward radial diffusion (Schulz & Lanzerotti, 1974). It is also proposed that when ~100 keV electrons interact with whistler-mode chorus waves, they can be accelerated to ~MeV energies (Boyd et al., 2014; Horne et al., 2005; Horne & Thorne, 1998; Li et al., 2007; Miyoshi et al., 2003; Reeves et al., 2013; Summers et al., 1998; Thorne et al., 2013). On the other hand, the loss of energetic electrons is typically attributed to three possible mechanisms: (i) adiabatic motion (ii) magnetopause shadowing, and (iii) precipitation into the atmosphere (Green et al., 2004).

The adiabatic electron losses are reversible in a sense that the particles are redistributed radially to conserve three adiabatic invariants (Dessler & Karplus, 1960; McIlwain, 1966). The increased ring current intensity during storm main phase decreases the magnetic flux, due to which the electrons are compelled to decelerate and move outward in order to conserve the first and third adiabatic invariants, respectively (Boynton et al., 2016; Ukhorskiy et al., 2006). This energetic electron flux returns to approximately the same location and energy once the ring current recovers after the storm (Kim & Chan, 1997).

Losses to the outer boundary, that is, the magnetopause, can occur when the magnetopause is displaced inward by increased solar wind pressure during a geomagnetic storm. Due to this, the electrons find themselves on open drift shells and can be lost to interplanetary space (Bortnik et al., 2006; Herrera et al., 2016; Kim et al., 2008). This effect is known as "magnetopause shadowing" (West et al., 1973).

Precipitation into the atmosphere can occur through resonant wave-particle interactions which decrease the electron's pitch angle. A variety of plasma waves have been identified, depending upon the region, time, and energy of the particles, which drive pitch angle scattering into the drift and bounce loss cone (Bortnik et al., 2006). This includes electromagnetic ion cyclotron (EMIC) waves (Clilverd et al., 2015; Miyoshi et al., 2008; Thorne et al., 2005), plasmaspheric ELF/VLF hiss (Lyons & Thorne, 1973), high-latitude VLF chorus (Behera et al., 2017), and electron cyclotron harmonic waves (Ni et al., 2012).

EMIC waves are pulsations in Pc1-2 having frequencies below proton gyrofrequency. These waves are generated near the field line magnetic equator (Fraser et al., 1996; Loto'Aniu et al., 2005) by unstable ion distributions in the ring current (Anderson & Hamilton, 1993; Cornwall, 1965). The waves can grow when strong temperature anisotropy exists ($T_{perp} > T_{par.}$) (Kozyra et al., 1984). The largest amplitude waves are seen in the dusk and dayside sectors at high L-shells ($L > 5$), and the occurrence rate is found to increase by up to a factor of five during major geomagnetic storms (Erlandson & Ukhorskiy, 2001). "Anomalous" gyroresonance between an electron and EMIC wave occurs when an electron overtakes a wave (Thorne & Kennel, 1971) so as to change the apparent polarization of the wave in the frame of electron. The typical resonant energies are >10 MeV in lower-density regions outside the plasmasphere and can drop to ≤1 MeV in regions like the plasmapause and in plasmaspheric plumes where the cold plasma electron density is relatively high (Meredith et al., 2003; Summers & Thorne, 2003; Thorne & Kennel, 1971; Ukhorskiy et al., 2010).

Plasmaspheric hiss is a broadband (~100 Hz–few kHz) VLF emission generated in the equatorial plane by the electron cyclotron instabilities (Thorne et al., 1973). These waves are found in high-density regions like the plasmasphere and plasmaspheric plumes. The highest amplitude waves are found in the dawn to evening sector. These waves allow resonance with ~MeV electrons below L~3 (Thorne et al., 1979).

Whistler-mode chorus waves are discrete emissions in the frequency range of ~100 Hz–5 kHz (Sazhin & Hayakawa, 1992) resulting from cyclotron instabilities (Kennel & Petschek, 1966) occurring near the geomagnetic equator in association with freshly injected plasma sheet electrons (Tsurutani & Smith, 1974). The chorus intensity increases during substorm activity and during the recovery phase of storms (Li et al., 2009; Meredith et al., 2001). Chorus waves, depending upon the electron energies, can accelerate or scatter these particles into the loss cone. The chorus wave can interact with 100 keV electrons in the ring current and outer radiation belt to accelerate the electrons to MeV energies (Horne & Thorne, 1998; Summers et al., 1998; Temerin et al., 1994).

The nonadiabatic loss processes of magnetopause shadowing and electron precipitation are the "true" losses of energetic electrons. Precipitation by resonant wave-particle interaction depends on particle energies, particle pitch angles, L-shells, plasma wave modes, frequencies, and intensities under different interplanetary and magnetospheric conditions (Tsurutani et al., 2016). The losses of energetic electron fluxes at the start of geomagnetic storm events are known as "dropouts" and are often rapid, that is, the flux can decrease by several orders of magnitude in a few hours. These dropout events are also defined as a flux decrease by factor of 4 in a day or a factor of 9 in two days where the decrease should account for at least a factor of 2.5 each day (Boynton et al., 2016). These sudden fluctuations in the flux are attributed to the above mentioned loss mechanisms, but the relative dominance of each mechanism likely varies from event to event.

Recently Shprits et al. (2017) have postulated that EMIC waves have the potential to precipitate relativistic electrons (2–6 MeV) from the outer radiation belt on rapid timescales and may be the dominant factor in the generation of radiation belt dropout events. Traditionally, EMIC waves are expected to precipitate electrons >1 MeV (Thorne & Kennel, 1971) although in the last few years, studies have shown that some EMIC waves can induce electron precipitation with energies of >200 keV (Hendry et al., 2017). There are very few studies on the estimation of the flux loss during dropouts as a result of relativistic electron precipitation. Recently, Zhang et al. (2017) estimated a net loss up to 6.8% of the 0.58–1.63 MeV electrons in a precipitation band event using conjunctive measurement of the Colorado Student Space Weather Experiment mission, the Balloon Array for Radiation belt Relativistic Electron Losses, and one of the Polar Operational Environmental Satellites. Previous analysis of nonrelativistic electron precipitation (typically 30 keV–1 MeV) using the NOAA POES satellites have shown that electron precipitation occurs typically 3 hours after the dropout and not during it (Hendry et al., 2012). The nonrelativistic precipitation appears to more likely to be linked to the period where the outer radiation belt electron fluxes are recovering as a result of acceleration processes.

It is unclear what fraction of the outer radiation belt flux is lost during dropout events through electron precipitation mechanisms. Baker et al. (2016) have speculated that the dropout of >1 MeV electrons on 17 March 2015 was due to magnetopause shadowing. However, radiation belt models have been found to underestimate the flux lost when applying only magnetopause shadowing effects to their simulations (Glauert et al., 2018). In this paper, we use ground-based subionospheric radio wave propagation observations to investigate the dropout event that occurred at ~06 UT on 17 March 2015 during the St. Patrick's Day storm. The dropout in relativistic electron flux levels was observed by the Van Allen Probes satellites. The focus of this work is to estimate the amount of relativistic electron flux precipitating into the atmosphere during the event, using ground-based subionospheric VLF receiver data. Rodger et al. (2012) have investigated the sensitivity of subionospheric VLF paths in the North American region by applying excess ionization generated by monoenergetic beams of precipitating electrons and power law spectrum, to the D-region during daytime and nighttime conditions. Their results show that the precipitation of >300 keV electrons exhibits large VLF amplitude and phase variations, and the technique is more sensitive during night as compared to daytime. The aim of this study is to investigate what fraction of the radiation belt relativistic electron flux has precipitated into the atmosphere so as to cause the observed VLF signal perturbations at $L \approx 3$–4.5. Section 2 describes the event and data sets available. Section 3 describes the satellite [3.1] and ground-based observations [3.2] prior to, and during, the dropout event. Section 4.1 models the electron density that reproduces the observed VLF perturbations during the dropout event. Section 4.2 determines the characteristics of the electron precipitation observed from the Van Allen Probes and compares them to those found in section 4.1 in order to determine the potential flux of precipitating relativistic electrons. Finally, section 5 estimates the fraction of trapped relativistic electron flux lost to the atmosphere during the dropout event.

2. Experimental Setup and Data

The solar cycle 24 started dramatically in 2009 after prolonged minima from 2006 to 2008. Surprisingly, there was not much geomagnetic activity even during the peak of the cycle until the first super geomagnetic storm in the declining phase of the cycle, on St. Patrick's day of 2015 with Dst = −223 nT. The two-step storm is thought to have been initiated by a halo coronal mass ejection, erupted from the Sun on 15 March 2015 (Wu et al., 2016). Figure 1 represents the interplanetary conditions on 17 March 2015. There is no data gap in ACE level 2 data, but there is a data gap from ~7 to 9 UT in the processed OMNI data. The Wind spacecraft recorded an interplanetary shock at 03:57 UT on the event day, and the arrival of the shock at the Earth produced a sudden storm commencement at 04:45 UT, represented by the vertical black line. The solar wind speed at that time showed an increase from ~400 km/s to ~500 km/s. Initially the IMF Bz was northward

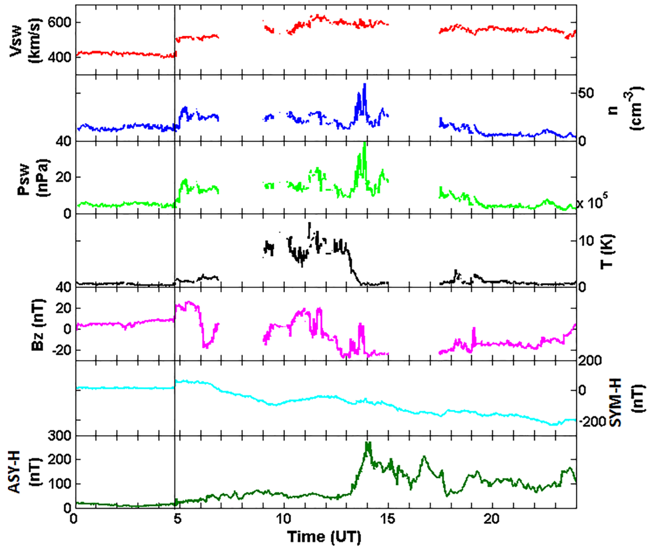

Figure 1. Interplanetary conditions measured during the period of interest in our study. This plot shows Wind observations representing solar wind speed (*Vsw*), density (*n*), pressure (*Psw*), temperature (*T*), IMF *Bz*, SYM-H, and ASY-H. The vertical black line represents the sudden storm commencement (SSC) which occurred at 04:45 UT.

until 05:00 UT and then turned southward to give Bz~−20 nT which decreased further as the storm progressed, and the solar wind speed increased to its maximum value of ~600 km/s. The main phase of the storm lasted about 18 hrs from ~6 to 23 UT on 17 March 2015.

To investigate the energetic electron precipitation into the atmosphere, narrowband VLF transmitter signals from NAA (44.6° N, 67.3°W) operating at a frequency of 24.0 kHz received at Seattle (47.9° N, 124.4°W) and Edmonton (53.35° N, 112.97° W) and the transmitter signals from NML (46.4° N, 98.3°W) operating at a frequency of 25.2 kHz received at St. John's (47.6° N, 52.7°W) and Edmonton are used. The great circle path lengths for NAA-Seattle are ~4305 km, NAA-Edmonton is ~3406 km, NML-St. John's is ~3410 km, and NML-Edmonton is ~1301 km, respectively. These transmitters and receivers are the part of the AARDDVARK network (Clilverd et al., 2009). More information about the network can be found at AARDDVARK homepage (http://www.physics.otago.ac.nz/space/AARDDVARK_homepage.htm). Figure 2 shows the transmitter-receiver sites with great circle paths and L = 3, 4, 5 contours. The subionospheric propagation paths are predominantly orientated east-west and can be used to remotely sense electron precipitation events at quasiconstant geomagnetic latitudes of L~3–4.5.

Some indication of the dynamic behavior of relativistic electron fluxes in the outer radiation belt during the main phase of the March 2015 storm can be determined from the POES SEM-2 telescope P6 (see Rodger et al., 2010 for a description of the instrument). Figure 3 shows the P6 trapped (upper panel) and bounce-loss-cone precipitating fluxes (lower panel) from all available POES observations during 17 March 2015. The color scale represents the logarithm of the flux levels. The vertical dashed lines represent the dropout period that will be investigated in this paper, that is, 06:30 to 08:30 UT, while the purple box represents the L-shell ranges for which VLF subionospheric narrowband data described in the paragraph above and is analyzed during the storm period. In the absence of

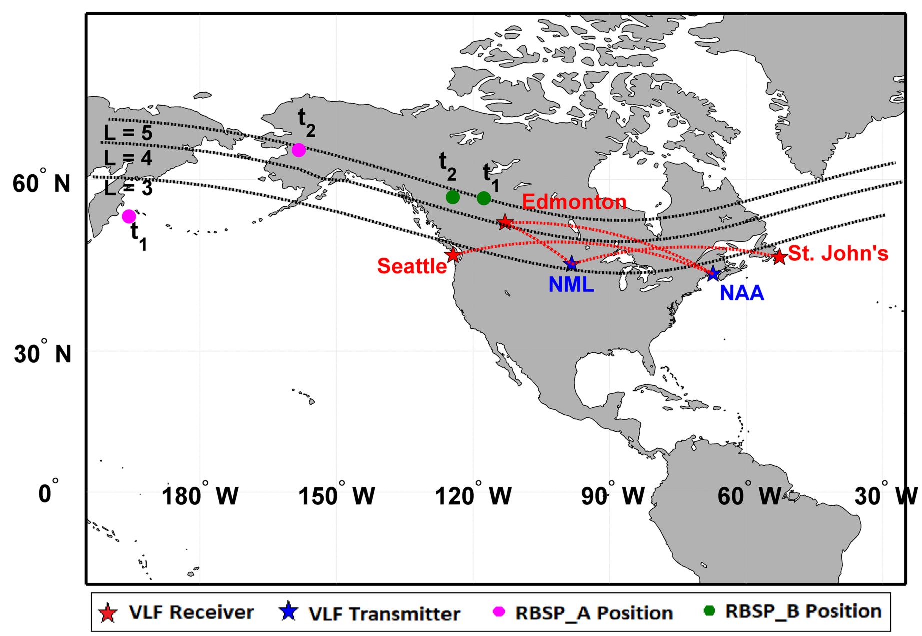

Figure 2. Locations of VLF transmitters, NAA, and NML and receivers Seattle (SEA), St. John's (STJ), and Edmonton (ED), respectively, along with great circle paths and L = 3, 4, 5 contours. The magenta and green dots represent the ionospheric footprints of RBSP-A and RBSP-B at t_1 = 6:30 UT and t_2 = 8:30 UT, respectively.

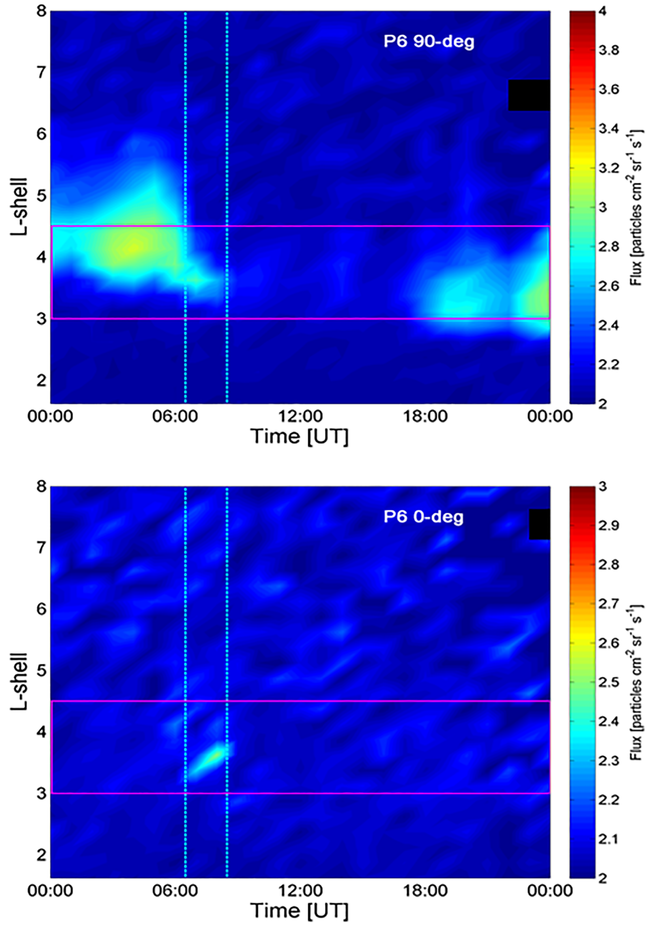

Figure 3. POES P6 trapped (90-deg) and BLC (0-deg) fluxes during 17 March 2015. The color bar shows the logarithm of the flux (for electron energy>700 keV), while the vertical dotted lines indicate the start and end times of the dropout event, and the horizontal red lines indicate the L-shell range of the VLF paths shown in Figure 2.

solar protons, the P6 telescope responds to electrons with energy >700 keV (Yando et al., 2011), and thus the figure indicates that relativistic trapped fluxes reduced over the L-shell range 3.5 to 5.5 at 06:30 UT (upper panel), while the only observable relativistic electron precipitation into the atmosphere occurred between 06:30 and 08:30 UT and in the L = 3.5 to 4.0 range (lower panel). We show the POES P6 channel as it is a direct measure of the electron precipitation flux relevant to the electron energies involved in relativistic electron flux dropouts (Baker et al., 2016) that are investigated in this paper, that is, >700 keV. The L-shell range over which the subionospheric VLF analysis will be performed in this study is well suited to investigate these regions. While the POES P6 telescope observed clear electron precipitation signatures at the time of the radiation belt dropout, the geometric factor of the P6 detector for electron "contamination" is complex and does not allow clear identification of the electron energies involved or what their flux levels might be. In order to investigate this event in more detail, we turn to the Van Allen Probes mission and its energetic electron telescopes.

The dropout in radiation belt energetic electron flux on 17 March 2015 was seen by the Relativistic Electron-Proton Telescope (REPT, ~MeV electrons) with supporting information provided by the Magnetic Electron Ion Spectrometer (MagEIS, ~keV electrons) instruments on board the Van Allen Probes (popularly known as RBSP). The RBSP consist of two probes, A and B, placed in very close orbits to study the events that occur simultaneously throughout the belts or localized at a point or which evolve with time from one point to another. The spacecrafts have nearly elliptical orbits lying in Earth's equatorial plane with ~20° inclination. The REPT and MagEIS form part of the energetic particle, composition, and thermal plasma suite which is dedicated to the measurement of particle energy and pitch angle. The REPT instrument measures the particles with relativistic energies, binned in 12 energy bands from 1.8 to 20 MeV. The MagEIS instrument measures the particles with lower energies, ranging from 31.5 keV to 4.2 MeV, distributed in 21 bins.

3. Observations

3.1. RBSP Energetic Electron Flux Observations

The ionospheric footprints of RBSP-A at time t_1 = 06:30 UT and t_2 = 08:30 UT are located at ~164.4°E and ~158.3°W and that of RBSP-B are at ~117.6°W and ~124.5°W, respectively as shown in Figure 2. A deep "dropout" of electrons with energies in the range 2.0–4.2 MeV was observed by REPT as shown in Figure 4 (panels a–f) during the main phase of the storm. Equivalent MagEIS observations are shown in Figure 4 (panels g–l). Figure 4 (panels a–c) represents the color-coded spin averaged intensities of REPT electrons with energies ~2.0, ~3.6, and ~ 4.2 MeV for March 2015. Figure 4 (panels d–f) is the zoomed views of panels a–c providing a closer look at 2 days around the time of the dropout that started at ~06:30 UT on 17 March. The flux decrease can be clearly seen from L = 3.5–6 in each energy range, but we restrict this study of the dropout at L~4 as the VLF perturbations are observed over $L \approx$ 3–4.5. The black vertical lines in the figure represent the duration of observed VLF perturbations as discussed later in this section, and we will focus on this time period throughout our further analysis in order to investigate the cause of the observed VLF perturbations.

The 2.0 MeV flux started to recover around 16:00 UT on 17 March 2015, whereas the higher energy flux (~4.2 MeV) did not recover until the early hours of 18 March 2015, coinciding with the main phase of the storm as mentioned in section 2. Figure 4 (panels g–i) shows the same format as panels a–c, but for MagEIS electrons of energies ~221, ~464, and ~741 keV, respectively, panels j–l provide a zoomed view of the same energy channels around the event time. There is no RBSP-A data available for ~221 keV channel. Although

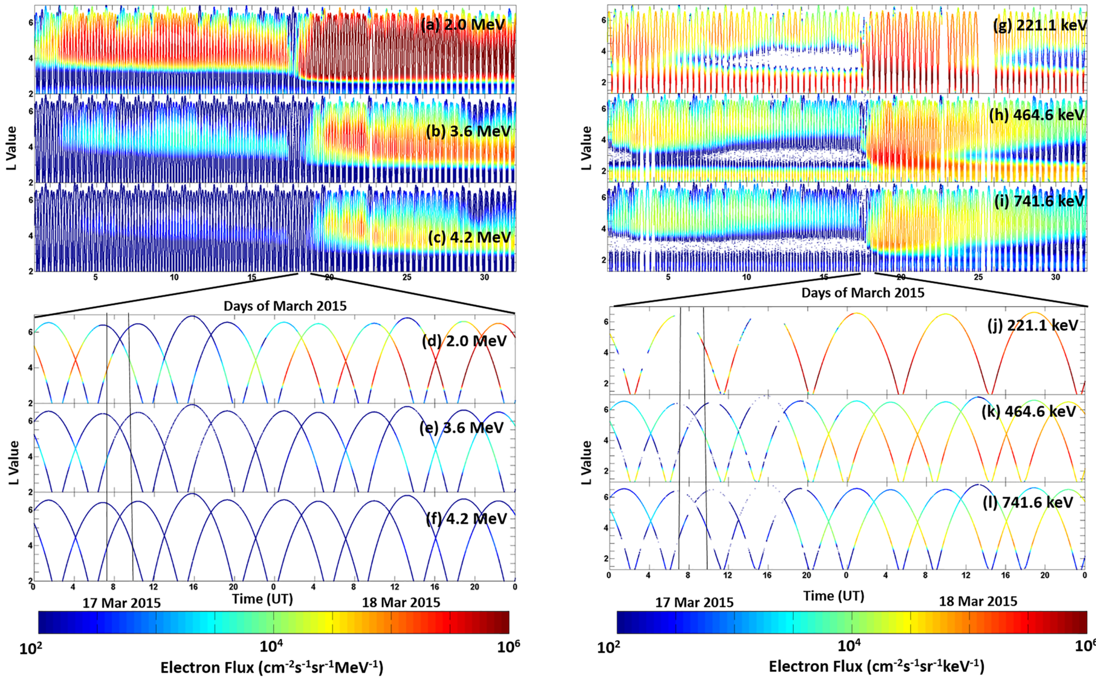

Figure 4. RBSP electron flux from relativistic electron proton telescope (REPT) for (a) 2.0, (b) 3.6, and (c) 4.2 MeV flux for whole month of March 2015; (d) 2.0, (e) 3.6, and (f) 4.2 MeV flux for 17 and 18 March 2015. RBSP electron flux from MagEIS for (g) 226.1, (h) 464.4, and (i) 741.6 keV flux for whole month of March 2015; and (j) 226.1, (k) 464.4, and (l) 741.6 keV flux for 17 and 18 March 2015. The vertical black lines represent the duration of VLF perturbations analyzed in this study.

enhancements in the MagEIS electron energies are observed as a result of the St. Patrick's day storm, there is no clear dropout event at energies of 226 keV; a dropout is seen for 464 keV at $L \approx 5$, while the 741 keV observations suggest that there is a small decrease in flux at the time of the dropout in already low flux levels occurring in the preceding days. Detailed inspection of the REPT and MagEIS channels suggests that the dropout in flux on 17 March 2015 is clearly discernible from $L = 3.5$–6 over energy ranges from 900 keV to 6.3 MeV. Based on the Van Allen Probes observations of those energy channels showing decreased flux levels during the dropout event, for the remainder of this study, we take the energy range of the EEP to span 900–6300 keV.

In order to determine the potential percentage of the total tube flux that could have been lost to the atmosphere during the flux dropout event, it is important to be able to determine the pitch angle distribution (α) at each energy in order to estimate the total tube content. It is also important to know the energy spectra of the precipitating flux in the bounce loss cone in order to be able to estimate the flux that produces the VLF perturbations—for this, we use pitch angle information as close to the bounce loss cone as possible. Figure 5 (panels a–e) represents the MagEIS pitch angle distribution for 2.0, 2.25, 2.85, 3.6, and 4.5 MeV electrons observed at 07:41 UT, 17 March 2015, as RBSP-A passed through the $L = 4$ flux tube, close to the magnetic field line equator. The timing is close to the start of the observed dropout event as shown in Figure 4. The pitch angle variation is given by a sinusoidal curve with $\sin^n\alpha$, where n takes values from 1 to 3 for 2.0 to 4.5 MeV, respectively, shown by a solid red curve in the figure. We also plot particle flux as a function of energy at 90° and 15° pitch angles (panel f). From the power law fit, it is seen that the power law gradient is −7.7 for 90° pitch angles, while it is −8.8 nearer to bounce loss cone (~6° at $L = 4$), that is, at 15° pitch angles. The next time that RBSP-A crossed the $L = 4$ field line was at 13:18 UT, which was close to the end of the observable dropout period and showed 95%–98% reductions in relativistic flux levels. These values will be used as an input to calculate ionospheric impact in section 4.2 of this paper and flux tube total content in section 5.

3.2. Perturbations in Narrowband VLF Transmitter Signals

VLF narrowband transmitter signals are a good tool to study any changes in the lowest region of the ionosphere that occur due to any forcing from above or below. The lower ionospheric changes are reflected as

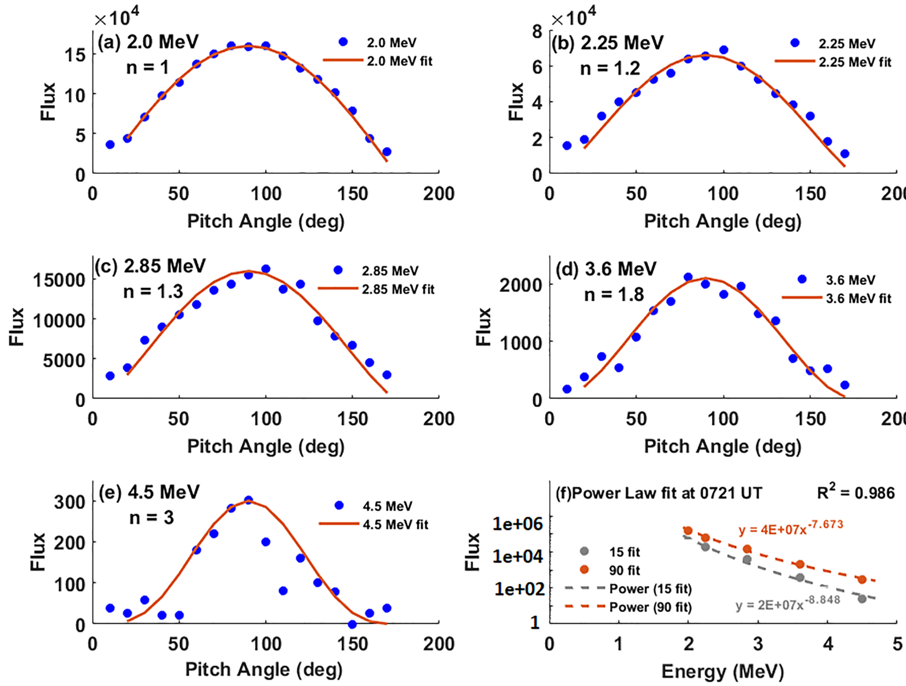

Figure 5. (panels a–e) RBSP-A pitch angle distributions for a range of relativistic electron energies at 07:21 UT at L = 4 on 17 March 2015. Labels indicate the *n* parameter fit (using $\sin^n\alpha$) to the observations. Panel f shows the power law energy spectrum at 90^0 and 15^0 pitch angles.

an increase or decrease in amplitude and phase of narrowband VLF transmitter signals. The VLF signals may incur amplitude and phase perturbations due to energetic electron precipitation (Clilverd et al., 2015; Rodger et al., 2008) which alters the ionospheric propagation conditions. In Figure 6, we show such subionospheric VLF data on 17 March 2015. We observe clear amplitude and phase perturbations just after the onset of the geomagnetic storm on 17 March 2015 in VLF transmitter signals received at Seattle and Edmonton from NAA and those received at St. John's and Edmonton from the NML transmitter. Figure 6a shows the amplitude (left-hand panels) and phase perturbations (right-hand panels) observed in the four paths over the whole day. The black curve is the signal on the disturbed day, whereas the red curve represents the quiet day curve of the narrowband VLF transmitter signal for respective paths. Asterisks represent radio wave propagation modeling (Ferguson, 1998) results for nondisturbed nighttime conditions (Thomson, Clilverd, et al., 2011; Thomson, Rodger, et al., 2011) and equivalent conditions during the day (Ferguson, 1998). Here we follow the technique of Thomson et al. (2007) and Thomson and McRae (2009) who use the relative phase and amplitude at night compared with the much more well-known conditions during the day (as they are driven by direct photoionization) in order to determine the ambient amplitude and phase levels during the pre-event (nighttime) period. Good agreement is seen between the modeling results and pre-event amplitude and phase values, suggesting that nondisturbed D-region profiles are a reasonable description of the pre-event conditions. The radio wave modeling will be discussed further in section 4.1.

In all of the panels of Figure 6a, we made some estimates of the variability of the nondisturbed amplitudes and phases in the observed values in 3 hours immediately prior to the dropout precipitation event. These are shown as green horizontal lines. We find that there could be an uncertainty in the amplitude of $+/-2.5$ dB and in phase of $+/-50^0$. These uncertainty limits will be taken into account in the determination of the drop-out perturbation size and in the resulting estimation of the likely D-region profile that the radio wave perturbations suggest (see section 4.1).

Figure 6b represents the amplitude (left-hand panels) and phase perturbations (right-hand panels) observed for all the four paths: NAA-Seattle, NML-St. John's, NAA- Edmonton, and NML-Edmonton, from 6 to 9 UT. The initial deviations from the respective quiet day curves in both amplitude and phase for both the paths

10.1029/2018JA026278

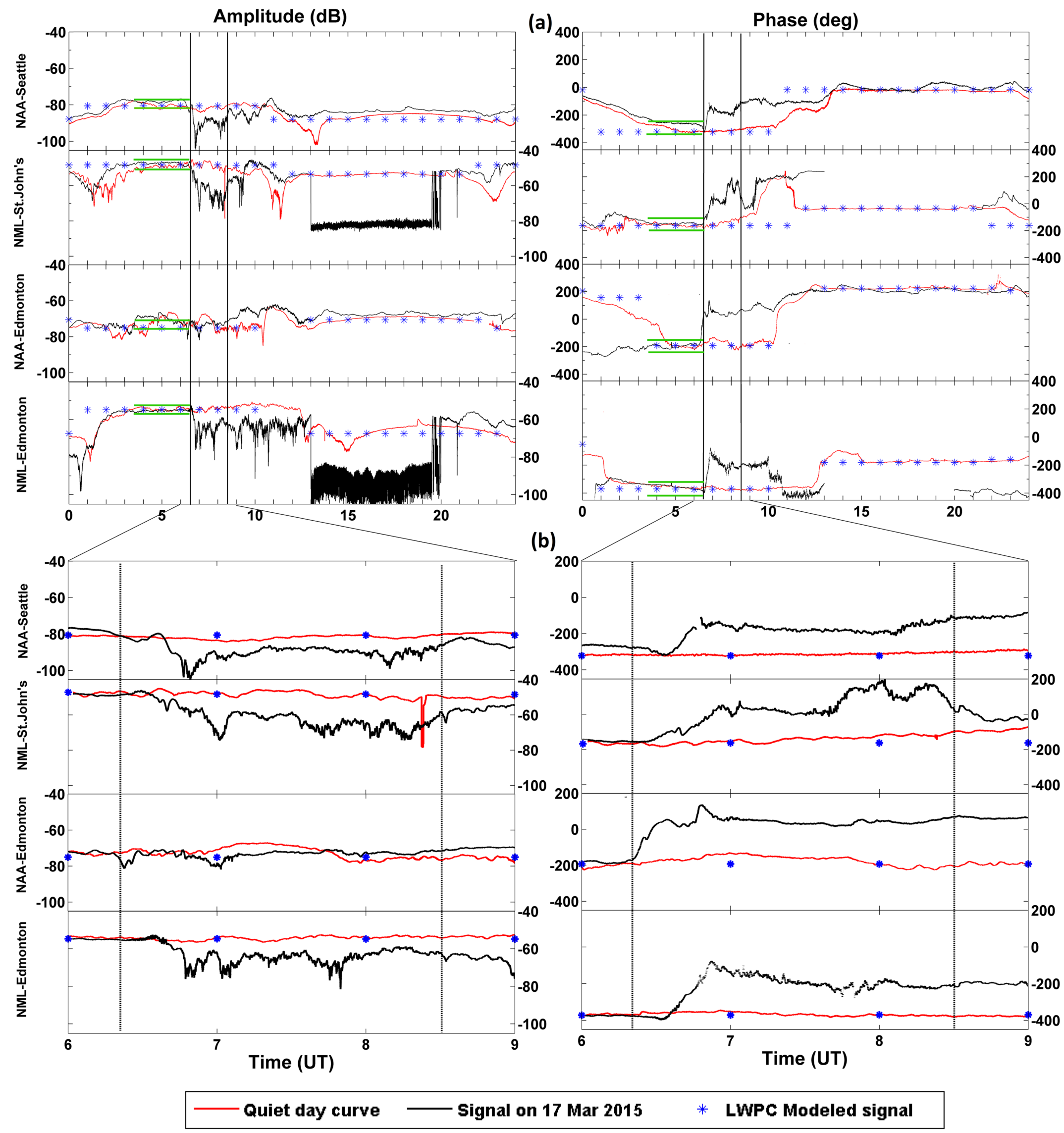

Figure 6. VLF amplitude (left-hand column) and phase (right-hand column) for the four paths studied (black lines). Panel (a) shows the data for 0–24 UT on 17 March 2015. Panel (b) shows the 6–9 UT period in more detail. Each individual path is identified on the left-hand side of the row. The red curves represent the signal observed on a representative nondisturbed day (marked as the "quiet day curve" (QDC)). Here the blue asterisks show the results of the LWPC modeling to reproduce the undisturbed QDC observations. Vertical black lines represent the duration over which average of the signal is taken. Horizontal green lines in panel (a) represents an estimate of the uncertainty in the pre-event amplitude and phase levels for 3 hours prior to the start time (see text for more details).

begin at ~6.3 UT. A sudden amplitude decrease of ~23+/−2.5 dB and an increase in phase by ~213+/−50^0 are observed for NAA-SEA around 6.8 UT. Similarly, a sudden amplitude decrease of ~27+/−2.5 dB and phase increase of ~218+/−50^0 are observed for NML-STJ around 7 UT. The VLF signal features an average decrease of ~8.5+/−2.5 and ~12.8+/−2.5 dB over both the paths, respectively, during the period of almost 2 hours from ~6.5 to 8.5 UT. This duration is shown by black vertical lines in Figure 6. During this period, the VLF signal showed an average phase increase of ~142+/−50^0, ~172+/−50^0, ~250+/−50^0, and ~180+/−50^0 for NAA-Seattle, NML-St. John's, NAA-Edmonton, and NML-Edmonton paths, respectively, starting around ~6.3 UT as shown by black dashed line in lower panel of Figure 6. The perturbations found in this study (10's of dB and several 100's of degrees) are of very similar size to the effects seen by a large range of published event studies, a subset of which include the effects of substorms (Clilverd et al., 2008, 2012), EMIC waves (Clilverd et al., 2015; Rodger et al., 2008), plasmaspheric hiss

(Hardman et al., 2015), and medium-large solar flares (Thomson et al., 2005). Therefore, while the perturbations during the dropout event are clear and substantial, they are consistent in size with the effects of many other relatively common phenomena and do not immediately suggest that a large portion of the radiation belt relativistic flux has been lost to the atmosphere during the dropout event. However, the coincidence of VLF perturbations during the main phase of the storm starting at the same time as the relativistic electron dropout event provides the motivation for the current study.

The effects of substantial precipitation occurring on the subionospheric path between Iceland and Sodankylä, Finland, ($L = 5.5$ to 6) were also seen, which show that the MLT region covered by the electron precipitation at least ranges from 00 to 08 MLT. In the case of the observations from NRK (37.5 kHz, Reykjavik, Iceland) to Sodankylä, Finland, the amplitude change at ~06 UT was ~−40 dB, pushing the signal into the noise floor, and as a result, the AARDDVARK receiver lost phase lock. Therefore, no estimate of the electron precipitation flux at L~6 could be made using those observations. We note, however, that the precipitation started at 06 UT at L~6, compared with ~6.3 UT at L~3−4, suggesting a delay in response at lower L-shells compared with higher L.

4. Modeling Results

4.1. LWPC Modeling

To infer the changes in the lower ionosphere on the event day, we first model the quiet time signal using the long wave propagation capability (LWPC) v 2.1 code developed by the US Naval Ocean System Center (Ferguson, 1998). This code calculates the full-wave reflection coefficients for the waveguide boundaries by taking into account the input path parameters. The process leads to the search for modal angles which give phase change of 2π across the guide taking into consideration the curvature of the Earth (Morfitt & Shellman, 1976). The program basically determines the upper boundary of the waveguide in terms of two "Wait parameters" used to describe the electron number density of the lower ionosphere through the sharpness factor, β (in km^{-1}), and reference height, $H^{/}$ (in km) (Wait & Spies, 1964). We use the LWPC code to determine the electron profile characteristics of the ionosphere that would have caused the VLF signal changes during the dropout event. For the undisturbed conditions (i.e., without additional electron precipitation), we use $\beta = 0.3\ km^{-1}$ and $H^{/} = 74$ km for daytime (12–23 UT) and $\beta = 0.63\ km^{-1}$ and $H^{/} = 85.1$ km for nighttime (0–11 UT) (Thomson et al., 2007; Thomson, Clilverd, et al., 2011; Thomson, Rodger, et al., 2011). The blue asterisks in Figure 6 represent the modeled signal. One can see that the modeled signal matches the quiet day curve shown by red and suggests that the pre-event conditions are well represented by nondisturbed D-region profiles that have previously been determined and extensively published in the past.

To further infer the ionospheric lower boundary conditions during the dropout event of 17 March 2015, the amplitude and phase perturbations of the VLF signal relative to the quiet day levels are plotted against $H^{/}$ for different values of β, for all four paths as shown in Figure 7. This exercise leads to the $H^{/}$ and β which would cause the observed perturbation in the VLF signal. The left panels show the amplitude and phase perturbations for the NAA-SEA and NAA-EDM subionospheric propagation paths, while the right panels show the equivalent results for the NML-STJ and NML-EDM propagation paths. The horizontal dot-dashed lines represent the experimentally observed changes in amplitude and phase on 17 March 2015 for each path, as mentioned in section 3.2. The vertical black line indicates the solution for $H^{/}$ that best matches the observed perturbation levels on the four paths. The green square centered on the crossing point of the two lines represents the upper and lower limits of the uncertainty in the perturbation levels due to uncertainty in the pre-event levels, as shown in Figure 6, and identifies the $H^{/}$ range that is necessary to take into account the perturbation uncertainty. It can be seen from the figure that $\beta = 0.35 \pm 0.05\ km^{-1}$ and $H^{/} = 80 \pm 1$ km would produce the observed changes in the VLF signals when uncertainty limits are taken into account. This solution explains the observed changes over all four paths, although in practice, there are a wider range of solutions that could describe the amplitude perturbation levels, and the result is primarily constrained by the phase perturbation levels. We further use this information to show that the shape of the precipitation-perturbed ionospheric profile determined from Van Allen Probes data is consistent with the beta/$H^{/}$ modeling profile found with the approach undertaken here and use it to calculate the equivalent relativistic flux that matches the beta/$H^{/}$ modeling profile that might be coming into the atmosphere during the dropout observed on 17 March 2015.

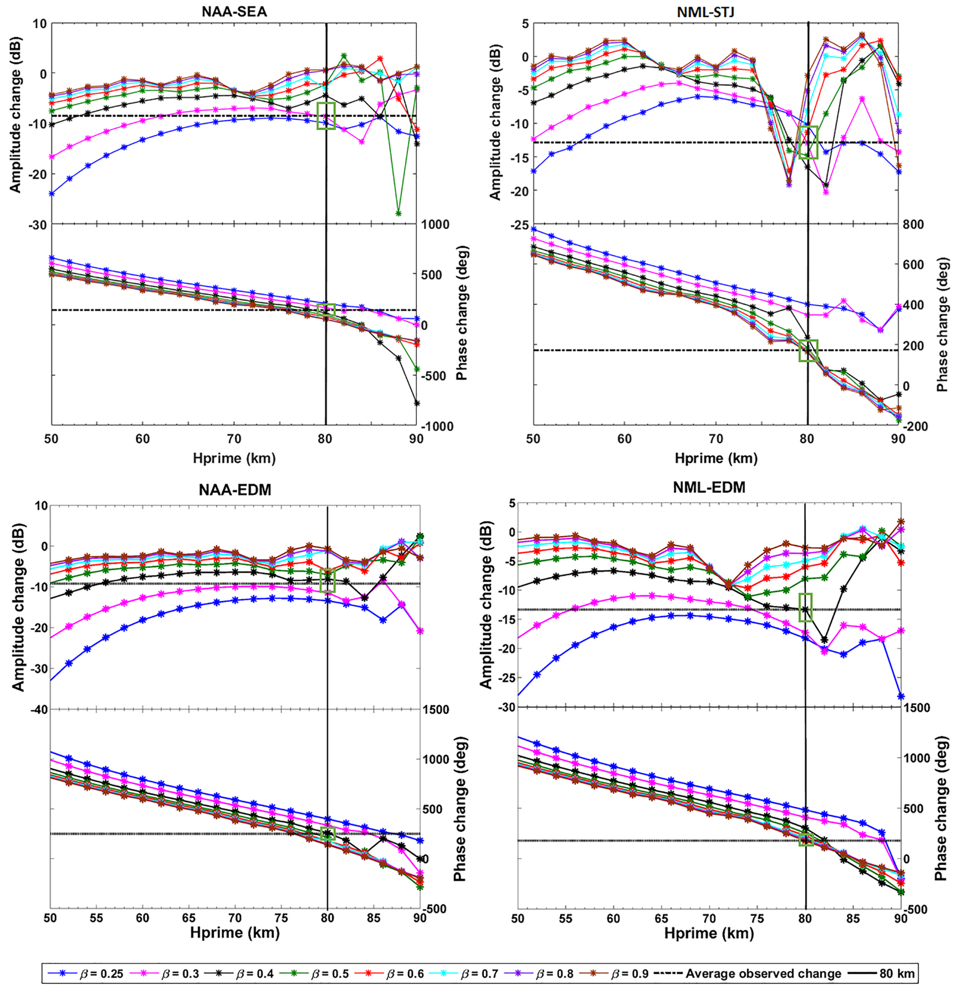

Figure 7. Variation of the LWPC modeled amplitude and phase of VLF signals as a function of the reference height ($H^{/}$) for varying sharpness factor (β) for the paths: NAA-SEA, NAA-EDM, NML-STJ, and NML-EDM. Observed perturbation levels on each path are indicated by horizontal dot-dashed lines, while the inferred $H^{/}$ solution is shown by a vertical line. The green boxes indicate the uncertainty in perturbation level and thus the $H^{/}$ solution due to uncertainty in the initial QDC levels (see text for more details).

4.2. Energetic Electron Precipitation (EEP) Modeling

From our earlier analysis, we know both the electron density profiles which describe (a) the undisturbed ionospheric D-region and (b) changes incurred by EEP during the dropout event. We also know parameters to describe the nature of electron flux lost from the outer radiation belt, potentially entering the ionosphere, that is, the energy range and pitch angle distribution. Our goal is to determine the magnitude of the EEP flux, such that we can estimate the importance of EEP to the observed dropout at *L*~4. We follow the same processes described in earlier studies to determine the EEP-affected electron density profiles (following, e.g., Rodger et al. (2013) and Simon-Wedlund et al. (2014)). The EEP-produced ionization rate is calculated for a range of EEP fluxes, assuming a power law energy spectrum with gradient −8.8 found in section 3.1. We assume the EEP spans the energy range of 900–6300 keV, based on the Van Allen Probes observations of which energy channels showed decreased flux levels during the dropout event, with the range bounded by the energy channels that did not show any flux decreases. From these ionization rates, the disturbed ionospheric electron density profile is determined, and the flux is identified which most closely produce the mid-range $\beta = 0.35$, $H^{/} = 80$ km profile determined in section 4.1.

The results of these calculations are shown in Figure 8. The undisturbed electron density profile is shown by the black line, representing a pre-event Wait ionosphere ($\beta = 0.63$, $H' = 85.1$ km) up to 90 km altitude, which

10.1029/2018JA026278

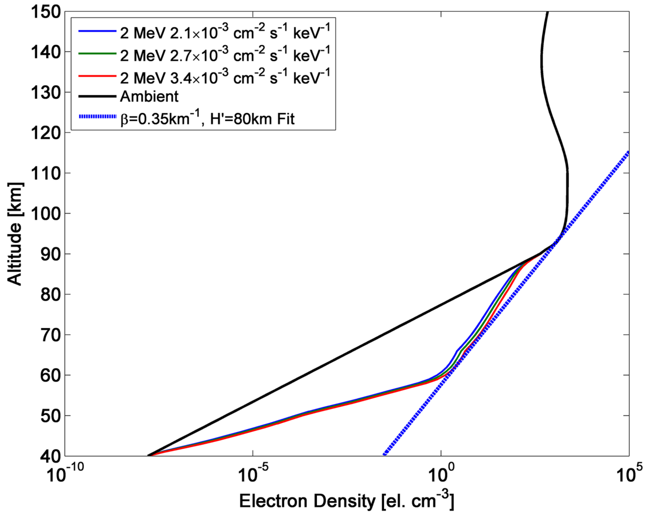

Figure 8. D-region electron number density profiles during the dropout event of 17 March 2015. The black line represents the ambient nighttime profile, while the heavy dashed blue line is the disturbed Wait ionosphere (β = 0.35, H′ = 80 km) inferred from the VLF observations. Lighter blue, green, and red lines are the best-fitting electron densities profiles produced by the EEP modeling determined from Van Allen Probes data for different flux levels.

then smoothly transitions to a profile provided by the international reference ionosphere (IRI-2007) appropriate for the middle of the propagation paths (50^0N, 270^0E). The heavy dashed blue line in Figure 8 is the disturbed Wait ionosphere ($\beta = 0.35$, $H' = 80$ km), while the lighter blue, green, and red lines are the best-fitting electron density profiles produced by the EEP modeling. We investigated the sensitivity of the EEP-produced electron number density profile to the choice of the ambient nighttime profile. In practice, the magnitude of the EEP-produced ionization is so dominant that it produces the same EEP ionization profile for a very wide range of ambient profiles, and thus although the VLF phase and amplitude analysis provides a clear indication of the nighttime ambient profile characteristics, it does not influence the final EEP ionization profile result significantly. Note that there is a fairly good agreement between the shape of the number density profiles produced by the EEP and the Wait ionosphere over the altitude range 55–90 km, inside which the VLF reflections will take place. Although the two profiles can be seen to diverge below number density levels of 10^{-1} el.cm^{-3} and the gradient becomes markedly steeper than ambient, the subionospheric VLF radio waves are insensitive to these densities and independent of the electron number density profile characteristics at these altitudes (<55 km) at night. While the EEP has an energy range starting at 900 keV, for the purpose of comparison with the dropout, we label these through their 2 MeV flux values. Those are 2.1×10^{-3} el.cm^{-2}s^{-1}keV^{-1}, 2.7×10^{-3} el.cm^{-2}s^{-1}keV^{-1}, and 3.4×10^{-3} el.cm^{-2}s^{-1}keV^{-1}, respectively.

5. Flux Tube Total Content Changes

Our goal is to determine how significant these EEP fluxes are to the observed electron flux dropout, that is, how much of the dropout is due to precipitation into the atmosphere. To do this, we calculate the total population of electrons in a flux tube at a given energy and determine the time required to deplete this tube to the RBSP-observed levels. This is a fairly common approach used in experimental studies to determine the overall significance of precipitation to the radiation belts (e.g., Blum et al., 2013; Lorentzen et al., 2001; O'Brien et al., 2004; Rodger et al., 2003; Voss et al., 1998).

As noted above, the D-region electron density profile consistent with the VLF observations can be produced by EEP with a relatively small range of flux magnitudes. For the purposes of the following comparison, we take the middle value. Note that this choice has no significant impact on the conclusions. At 0724 UT, near the beginning of the dropout, RBSP-A passed through $L = 4$ and determined the trapped 2 MeV flux and pitch angle distribution, as described above. We use this information to determine the number of 2 MeV electrons in a magnetic flux tube of 1 square centimeter in area at the equatorial plane and then transform this value to the top of atmosphere at 100 km (in both cases following the methodology described by Voss et al. (1998) and Rodger et al. (2003)). This leads to a flux tube total 2 MeV electron population of 1.2×10^4 electrons. In contrast, at 1318 UT, near the end of the dropout, the RBSP observations indicate the flux tube total 2 MeV electron population was 695 electrons. From this, we see that there was a ~95% decrease in the total flux tube content at this energy. However, the EEP at 2 MeV that we have calculated above would take slightly more than 50 days to cause such a large decrease. As the ~95% decrease occurred in ~7 hours, it is clear that very little of the dropout can be explained through precipitation into the atmosphere. At the specific EEP rate, we would expect the total tube content to only decrease by <0.5%, by considering the 900–6300 keV electron flux.

We have also undertaken the same calculation for 3.6 MeV, where the dropout was >98%. For the VLF-determined EEP rate, it would take 45 days to drain the flux tube content to this level, again, vastly longer than experimentally observed. If some of the VLF phase and amplitude perturbations are due to the precipitation of electrons with lower electron energy (i.e., <900 keV), then the flux of 900–6300 keV electrons that we calculate here would consequently be even smaller than stated. Therefore, in this study, the maximum loss of 900–6300 keV electrons that could have occurred during the dropout event is determined, and it could potentially be smaller than this. We note that precipitation at lower energies than the relativistic ones assumed here could have influenced the size of the radio wave perturbations. Thus, the flux of relativistic electrons that have been determined in this study could have been even smaller than those calculated as a result of our working assumption (i.e., that all of the perturbation was due to relativistic flux). There is even the possibility that the entire VLF perturbation observed could have been generated by lower energy precipitation (100's of keV or so) such that there was no relativistic precipitation involved in the observed perturbations. However, this is unlikely due to the fact that some relativistic electron precipitation was observed by the POES satellites at the beginning of the dropout period. Thus, this study calculates an upper limit of the likely relativistic fluxes involved. From this, we conclude that EEP played only a very small role in the observed electron flux dropout.

6. Discussion and Summary

Many previous studies have focused on the loss mechanism of outer belt electron flux (Baker et al., 2016; Dessler & Karplus, 1960; Imhof & Gaines, 1993; Thorne et al., 2005; Ukhorskiy et al., 2006; West et al., 1973), but very few of them gave attention to relative contribution of each physical mechanism (Bortnik et al., 2006; Li et al., 1997; Morley et al., 2010; Onsager et al., 2002; Xiang et al., 2017; Yu et al., 2013). In this paper, we have determined the fraction of the outer belt relativistic electrons at L~4 that could have precipitated into the atmosphere during the dropout event that occurred during the St. Patrick's Day storm of 2015. We assume that the perturbations observed on ground-based narrowband VLF radio waves are entirely due to relativistic electron precipitation associated with the dropout observed by the Van Allen probes and thus calculate an upper limit of the likely relativistic fluxes involved. A dropout of electrons with energies in the range from 900 keV to 6.3 MeV was seen through RBSP's flux measurements starting at ~0630 UT on 17 March 2015 over L = 3.5–6 with a power law energy spectral gradient of −8.8 at 15° pitch angle, that is, close to the atmospheric loss cone. Strong perturbations in VLF narrowband transmitter signals for four $L \approx 3$ to 4.5 paths, that is, NAA-Seattle, NAA-Edmonton, NML-St. John's and NML-Edmonton, are observed for nearly 2 hours starting at the same time as the dropout. Phase increases of ~180° are typically observed on the four paths analyzed from ~0630 to 0830 UT. LWPC modeling is performed to infer the ionospheric changes that occurred at the time of the dropout, using Wait ionospheric parameterization. We found that $\beta = 0.35\ \mathrm{km}^{-1}$ and $H' = 80$ km would produce the observed changes in VLF signal. The power law gradient and pitch angle distributions from RBSP, as well as Wait ionospheric parameters from VLF radio wave observations, are used to calculate total tube content and subsequent EEP loss rates. The results suggest that it would take 50 days to drain a flux tube of 2 MeV electrons and 45 days to drain the 3.6 MeV flux at $L \approx 4$. However, the satellite observations suggest that the flux decrease to drain the flux tube by 95% only took ~7 hours. Our calculations indicate that during this time interval only <0.5% of the relativistic fluxes (900–6300 keV) could have been lost to the atmosphere. This leads to the conclusion that a very minimal fraction of the total trapped relativistic flux entered the atmosphere as a result of the dropout at L = 3–4.5, and electron precipitation was not the major contributor to the observed dropout during the St. Patrick's Day storm of 2015.

Acknowledgments
SAG benefited from the SCOSTEP Visiting Scholar Program, under which she visited South African National Space Agency (SANSA), South Africa, where this research was initiated. SAG would like to thank Tongji University for the postdoctoral fund. SAG also thanks Claudia Martinez (ISEE, Nagoya University) for her timely technical help. Authors from Indian Institute of Geomagnetism (IIG) are grateful to Director, IIG, for support and encouragement to carry out the work. We thank ACE, Wind, and OMNIWeb (https://omniweb.gsfc.nasa.gov/form/dx1.html) teams for providing solar wind data. We acknowledge the RBSP data providers J. Bernard Blake (The Aerospace Corporation) and D. Baker (University of Colorado at Boulder). This data can be found on CDAWeb (https://cdaweb.sci.gsfc.nasa.gov/). The subionospheric VLF data can be found at the Polar Data Centre (http://psddb.data/data/access/coverage.php?menu=1,7&bc=1&source=1&class=232&type=ULTRA). The authors would also like to acknowledge useful discussions with Alyson Jaynes regarding the RBSP data analysis. MAC would like to acknowledge grant sponsored from the Natural Environment Research Council (UKRI-NERC) Highlight Topic grant number NE/P01738X/1 (Rad-Sat) and the Royal Society Newton Fund International exchanges award 2015.

References

Anderson, B. J., & Hamilton, D. C. (1993). Electromagnetic ion cyclotron waves stimulated by modest magnetospheric compressions. *Journal of Geophysical Research*, *98*(A7), 11,369–11,382. https://doi.org/10.1029/93JA00605

Baker, D. N., Jaynes, A. N., Kanekal, S. G., Foster, J. C., Erickson, P. J., Fennell, J. F., & Henderson, M. G. (2016). Highly relativistic radiation belt electron acceleration, transport, and loss: Large solar storm events of March and June 2015. *Journal of Geophysical Research: Space Physics*, *121*, 6647–6660. https://doi.org/10.1002/2016JA022502

Behera, J. K., Sinha, A. K., Vichare, G., Bhaskar, A., Honary, F., Rawat, R., & Singh, R. (2017). Enhancement and modulation of cosmic noise absorption in the afternoon sector at subauroral location (L = 5) during the recovery phase of 17 March 2015 geomagnetic storm. *Journal of Geophysical Research: Space Physics*, *122*, 9528–9544. https://doi.org/10.1002/2017JA024226

Blum, L. W., Schiller, Q., Li, X., Millan, R., Halford, A., & Woodger, L. (2013). New conjunctive CubeSat and balloon measurements to quantify rapid energetic electron precipitation. *Geophysical Research Letters*, *40*, 5833–5837. https://doi.org/10.1002/2013GL058546

Bortnik, J., Thorne, R. M., O'Brien, T. P., Green, J. C., Strangeway, R. J., Shprits, Y. Y., & Baker, D. N. (2006). Observation of two distinct, rapid loss mechanisms during the 20 November 2003 radiation belt dropout event. *Journal of Geophysical Research*, *111*, A12216. https://doi.org/10.1029/2006JA011802

Boyd, A. J., Spence, H. E., Claudepierre, S. G., Fennell, J. F., Blake, J. B., Baker, D. N., et al. (2014). Quantifying the radiation belt seed population in the 17 March 2013 electron acceleration event. *Geophysical Research Letters*, *41*, 2275–2281. https://doi.org/10.1002/2014GL059626

Boynton, R. J., Mourenas, D., & Balikhin, M. A. (2016). Electron flux dropouts at geostationary Earth orbit: Occurrences, magnitudes, and main driving factors. *Journal of Geophysical Research: Space Physics*, *121*, 8448–8461. https://doi.org/10.1002/2016JA022916

Clilverd, M. A., Duthie, R., Hardman, R., Hendry, A. T., Rodger, C. J., Raita, T., & Milling, D. K. (2015). Electron precipitation from EMIC waves: A case study from 31 May 2013. *Journal of Geophysical Research: Space Physics*, *120*, 3618–3631. https://doi.org/10.1002/2015JA021090

Clilverd, M. A., Rodger, C. J., Brundell, J. B., Cobbett, N., Bähr, J., Moffat-Griffin, T., et al. (2008). Energetic electron precipitation during sub-storm injection events: High-latitude fluxes and an unexpected mid-latitude signature. *Journal of Geophysical Research*, *113*, A10311. https://doi.org/10.1029/2008JA013220

Clilverd, M. A., Rodger, C. J., Danskin, D., Usanova, M. E., Raita, T., Ulich, T., & Spanswick, E. L. (2012). Energetic particle injection, acceleration, and loss during the geomagnetic disturbances which upset Galaxy 15. *Journal of Geophysical Research*, *117*, A12213. https://doi.org/10.1029/2012JA018175

Clilverd, M. A., Rodger, C. J., Thomson, N. R., Brundell, J. B., Ulich, T., Lichtenberger, J., et al. (2009). Remote sensing space weather events: Antarctic-Arctic radiation-belt (dynamic) deposition-VLF atmospheric research Konsortium network. *Space Weather*, *7*, S04001. https://doi.org/10.1029/2008SW000412

Cornwall, J. M. (1965). Cyclotron instabilities and electromagnetic emission in the ultralow frequency and very low frequency ranges. *Journal of Geophysical Research*, *70*(1), 61–69. https://doi.org/10.1029/JZ070i001p00061

Dessler, A. J., & Karplus, R. (1960). Some properties of the Van Allen radiation. *Physical Review Letters*, *4*(6), 271–274. https://doi.org/10.1103/PhysRevLett.4.271

Erlandson, R. E., & Ukhorskiy, A. J. (2001). Observations of electromagnetic ion cyclotron waves during geomagnetic storms: Wave occurrence and pitch angle scattering. *Journal of Geophysical Research*, *106*(A3), 3883–3895. https://doi.org/10.1029/2000JA000083

Ferguson, J. A. (1998). *Computer programs for assessment of long-wavelength radio communications, Version 2.0: User's guide and source files*, (Vol. TD-3030). San Diego, CA: Space and naval warfare systems center.

Fraser, B. J., Singer, H. J., Hughes, W. J., Wygant, J. R., Anderson, R. R., & Hu, Y. D. (1996). CRRES Poynting vector observations of electromagnetic ion cyclotron waves near the plasmapause. *Journal of Geophysical Research*, *101*(A7), 15,331–15,343. https://doi.org/10.1029/95JA03480

Glauert, S. A., Horne, R. B., & Meredith, N. P. (2018). A 30-year simulation of the outer electron radiation belt. *Space Weather*, *16*, 1498–1522. https://doi.org/10.1029/2018SW001981

Green, J. C., Onsager, T. G., O'Brien, T. P., & Baker, D. N. (2004). Testing loss mechanisms capable of rapidly depleting relativistic electron flux in the Earth's outer radiation belt. *Journal of Geophysical Research*, *109*, A12211. https://doi.org/10.1029/2004JA010579

Hardman, R., Clilverd, M. A., Rodger, C. J., Brundell, J. B., Duthie, R., Holzworth, R. H., et al. (2015). A case study of electron precipitation fluxes due to plasmaspheric hiss. *Journal of Geophysical Research: Space Physics*, *120*, 6736–6748. https://doi.org/10.1002/2015JA021429

Hendry, A. T., Rodger, C. J., & Clilverd, M. A. (2017). Evidence of sub–MeV EMIC–driven electron precipitation. *Geophysical Research Letters*, *44*, 1210–1218. https://doi.org/10.1002/2016GL071807

Hendry, A. T., Rodger, C. J., Clilverd, M. A., Thomson, N. R., Morley, S. K., & Raita, T. (2012). Rapid radiation belt losses occurring during high speed solar wind stream driven storms: Importance of energetic electron precipitation. *Dynamics of the Earth's Radiation Belts and Inner Magnetosphere*, *199*, 213–223. https://doi.org/10.1029/2012GM001299

Herrera, D., Maget, V. F., & Sicard-Piet, A. (2016). Characterizing magnetopause shadowing effects in the outer electron radiation belt during geomagnetic storms. *Journal of Geophysical Research: Space Physics*, *121*, 9517–9530. https://doi.org/10.1002/2016JA022825

Horne, R. B., & Thorne, R. M. (1998). Potential waves for relativistic electron scattering and stochastic acceleration during magnetic storms. *Geophysical Research Letters*, *25*(15), 3011–3014. https://doi.org/10.1029/98GL01002

Horne, R. B., Thorne, R. M., Glauert, S. A., Albert, J. M., Meredith, N. P., & Anderson, R. R. (2005). Timescale for radiation belt electron acceleration by whistler mode chorus waves. *Journal of Geophysical Research*, *110*, A03225. https://doi.org/10.1029/2004JA010811

Imhof, W. L., & Gaines, E. E. (1993). Inputs to the atmosphere from relativistic electrons. *Journal of Geophysical Research*, *98*(A8), 13,575–13,580. https://doi.org/10.1029/93JA01149

Kennel, C. F., & Petschek, H. E. (1966). Limit on stably trapped particle fluxes. *Journal of Geophysical Research*, *71*(1), 1–28. https://doi.org/10.1029/JZ071i001p00001

Kim, H. J., & Chan, A. A. (1997). Fully adiabatic changes in storm time relativistic electron fluxes. *Journal of Geophysical Research*, *102*(A10), 22,107–22,116. https://doi.org/10.1029/97JA01814

Kim, K. C., Lee, D. Y., Kim, H. J., Lyons, L. R., Lee, E. S., Öztürk, M. K., & Choi, C. R. (2008). Numerical calculations of relativistic electron drift loss effect. *Journal of Geophysical Research*, *113*, A09212. https://doi.org/10.1029/2007JA013011

Kivelson, M. G., & Russell, C. T. (Eds) (1995). *Introduction to space physics*. Cambridge: Cambridge University Press.

Kozyra, J. U., Cravens, T. E., Nagy, A. F., Fontheim, E. G., & Ong, R. S. B. (1984). Effects of energetic heavy ions on electromagnetic ion cyclotron wave generation in the plasmapause region. *Journal of Geophysical Research*, *89*(A4), 2217–2233. https://doi.org/10.1029/JA089iA04p02217

Li, W., Shprits, Y. Y., & Thorne, R. M. (2007). Dynamic evolution of energetic outer zone electrons due to wave–particle interactions during storms. *Journal of Geophysical Research*, *112*, A10220. https://doi.org/10.1029/2007JA012368

Li, W., Thorne, R. M., Angelopoulos, V., Bortnik, J., Cully, C. M., Ni, B., & Magnes, W. (2009). Global distribution of whistler–mode chorus waves observed on the THEMIS spacecraft. *Geophysical Research Letters*, *36*, L09104. https://doi.org/10.1029/2009GL037595

Li, X., Baker, D. N., Temerin, M., Caytone, T. E., Reeves, E. G. D., Christensen, R. A., et al. (1997). Multisatellite observations of the outer zone electron variation during the 3–4 November 1993 magnetic storm. *Journal of Geophysical Research*, *102*(A7), 14,123–14,140. https://doi.org/10.1029/97JA01101

Lorentzen, K. R., Looper, M. D., & Blake, J. B. (2001). Relativistic electron microbursts during the GEM storms. *Geophysical Research Letters*, *28*(13), 2573–2576. https://doi.org/10.1029/2001GL012926

Loto'Aniu, T. M., Fraser, B. J., & Waters, C. L. (2005). Propagation of electromagnetic ion cyclotron wave energy in the magnetosphere. *Journal of Geophysical Research*, *110*, A07214. https://doi.org/10.1029/2004JA010816

Lyons, L. R., & Thorne, R. M. (1973). Equilibrium structure of radiation belt electrons. *Journal of Geophysical Research*, *78*(13), 2142–2149. https://doi.org/10.1029/JA078i013p02142

Mauk, B. H., Fox, N. J., Kanekal, S. G., Kessel, R. L., Sibeck, D. G., & Ukhorskiy, A. (2012). Science objectives and rationale for the radiation belt storm probes mission. In *The Van Allen Probes Mission*, (pp. 3–27). Boston, MA: Springer. https://doi.org/10.1007/s11214-012-9908-y

McIlwain, C. E. (1966). Ring current effects on trapped particles. *Journal of Geophysical Research*, *71*(15), 3623–3628. https://doi.org/10.1029/JZ071i015p03623

Meredith, N. P., Horne, R. B., & Anderson, R. R. (2001). Substorm dependence of chorus amplitudes: Implications for the acceleration of electrons to relativistic energies. *Journal of Geophysical Research*, *106*(A7), 13,165–13,178. https://doi.org/10.1029/2000JA900156

Meredith, N. P., Thorne, R. M., Horne, R. B., Summers, D., Fraser, B. J., & Anderson, R. R. (2003). Statistical analysis of relativistic electron energies for cyclotron resonance with EMIC waves observed on CRRES. *Journal of Geophysical Research*, *108*(A6), 1250. https://doi.org/10.1029/2002JA009700

Millan, R. M., & Thorne, R. M. (2007). Review of radiation belt relativistic electron losses. *Journal of Atmospheric and Solar-Terrestrial Physics*, *69*(3), 362–377. https://doi.org/10.1016/j.jastp.2006.06.019

Miyoshi, Y., Morioka, A., Misawa, H., Obara, T., Nagai, T., & Kasahara, Y. (2003). Rebuilding process of the outer radiation belt during the 3 November 1993 magnetic storm: NOAA and Exos–D observations. *Journal of Geophysical Research*, *108*(A1), SMP-3), 1004. https://doi.org/10.1029/2001JA007542

Miyoshi, Y., Sakaguchi, K., Shiokawa, K., Evans, D., Albert, J., Connors, M., & Jordanova, V. (2008). Precipitation of radiation belt electrons by EMIC waves, observed from ground and space. *Geophysical Research Letters*, *35*, L23101. https://doi.org/10.1029/2008GL035727

Morfitt, D. G., and Shellman, C. H. (1976). 'MODESRCH', An improved computer program for obtaining ELF/VLF/LF mode constants in an Earth ionosphere waveguide (No. NELC/IR-77 T). Naval Electronics Lab Center San Diego CA.

Morley, S. K., Friedel, R. H. W., Spanswick, E. L., Reeves, G. D., Steinberg, J. T., Koller, J., et al. (2010). Dropouts of the outer electron radiation belt in response to solar wind stream interfaces: Global positioning system observations. *Proceedings of the Royal Society of London, Series A*, *466*(2123), 3329–3350. https://doi.org/10.1098/rspa.2010.0078

Ni, B., Liang, J., Thorne, R. M., Angelopoulos, V., Horne, R. B., Kubyshkina, M., et al. (2012). Efficient diffuse auroral electron scattering by electrostatic electron cyclotron harmonic waves in the outer magnetosphere: A detailed case study. *Journal of Geophysical Research*, *117*(A1), A01218. https://doi.org/10.1029/2011JA017095

O'Brien, T. P., Looper, M. D., & Blake, J. B. (2004). Quantification of relativistic electron microburst losses during the GEM storms. *Geophysical Research Letters*, *31*, L04802. https://doi.org/10.1029/2003GL018621

Onsager, T. G., Rostoker, G., Kim, H.-J., Reeves, G. D., Obara, T., Singer, H. J., & Smithtro, C. (2002). Radiation belt electron flux dropouts: Local time, radial, and particle-energy dependence. *Journal of Geophysical Research*, *107*(A11), 1382. https://doi.org/10.1029/2001JA000187

Reeves, G. D., McAdams, K. L., Friedel, R. H. W., & O'Brien, T. P. (2003). Acceleration and loss of relativistic electrons during geomagnetic storms. *Geophysical Research Letters*, *30*(10), 1529. https://doi.org/10.1029/2002GL016513

Reeves, G. D., Spence, H. E., Henderson, M. G., Morley, S. K., Friedel, R. H. W., Funsten, H. O., & Claudepierre, S. G. (2013). Electron acceleration in the heart of the Van Allen radiation belts. *Science*, *341*(6149), 991–994. https://doi.org/10.1126/science.1237743

Rodger, C. J., Clilverd, M. A., Green, J., & Lam, M.-M. (2010). Use of POES SEM-2 observations to examine radiation belt dynamics and energetic electron precipitation into the atmosphere. *Journal of Geophyscal Research: Space Physics*, *115*, A04202. https://doi.org/10.1029/2008JA014023

Rodger, C. J., Clilverd, M. A., Kavanagh, A. J., Watt, C. E., Verronen, P. T., & Raita, T. (2012). Contrasting the responses of three different ground–based instruments to energetic electron precipitation. *Radio Science*, *47*, RS2021. https://doi.org/10.1029/2011RS004971

Rodger, C. J., Clilverd, M. A., & McCormick, R. J. (2003). Significance of lightning-generated whistlers to inner radiation belt electron lifetimes. *Journal of Geophysical Research*, *108*(A12), 1462. https://doi.org/10.1029/2003JA009906

Rodger, C. J., Kavanagh, A. J., Clilverd, M. A., & Marple, S. R. (2013). Comparison between POES energetic electron precipitation observations and riometer absorptions: Implications for determining true precipitation fluxes. *Journal of Geophysical Research: Space Physics*, *118*, 7810–7821. https://doi.org/10.1002/2013JA019439

Rodger, C. J., Raita, T., Clilverd, M. A., Seppälä, A., Dietrich, S., Thomson, N. R., & Ulich, T. (2008). Observations of relativistic electron precipitation from the radiation belts driven by EMIC waves. *Geophysical Research Letters*, *35*, L16106. https://doi.org/10.1029/2008GL034804

Sazhin, S. S., & Hayakawa, M. (1992). Magnetospheric chorus emissions: A review. *Planetary and Space Science*, *40*(5), 681–697. https://doi.org/10.1016/0032-0633(92)90009-D

Schulz, M., & Lanzerotti, L. J. (1974). *Particle diffusion in the radiation belts*, (Vol. 7). Springer, Berlin, Heidelberg: Springer Science and Business Media. https://doi.org/10.1007/978-3-642-65675-0

Shprits, Y. Y., Kellerman, A., Aseev, N., Drozdov, A. Y., & Michaelis, I. (2017). Multi–MeV electron loss in the heart of the radiation belts. *Geophysical Research Letters*, *44*, 1204–1209. https://doi.org/10.1002/2016GL072258

Simon-Wedlund, M., Clilverd, M. A., Rodger, C. J., Cresswell-Moorcock, K., Cobbett, N., Breen, P., et al. (2014). A statistical approach to determining energetic outer radiation belt electron precipitation fluxes. *Journal of Geophysical Research: Space Physics*, *119*, 3961–3978. https://doi.org/10.1002/2013JA019715

Summers, D., & Thorne, R. M. (2003). Relativistic electron pitch–angle scattering by electromagnetic ion cyclotron waves during geomagnetic storms. *Journal of Geophysical Research*, *108*(A4), 1143. https://doi.org/10.1029/2002JA009489

Summers, D., Thorne, R. M., & Xiao, F. (1998). Relativistic theory of wave–particle resonant diffusion with application to electron acceleration in the magnetosphere. *Journal of Geophysical Research*, *103*(A9), 20,487–20,500. https://doi.org/10.1029/98JA01740

Temerin, M., Roth, I., Hudson, M. K., & Wygant, J. R. (1994). New paradigm for the transport and energization of radiation belt particles. *Eos, Transactions American Geophysical Union*, *75*(44), 538.

Thomson, N. R., Clilverd, M. A., & McRae, W. M. (2007). Nighttime ionospheric D region parameters from VLF phase and amplitude. *Journal of Geophysical Research*, *112*, A07304. https://doi.org/10.1029/2007JA012271

Thomson, N. R., Clilverd, M. A., & Rodger, C. J. (2011). Daytime mid-latitude D region parameters at solar minimum from short path VLF phase and amplitude. *Journal of Geophysical Research*, *116*, A03310. https://doi.org/10.1029/2010JA016248

Thomson, N. R., & McRae, W. M. (2009). Nighttime ionospheric D region: Equatorial and non-equatorial. *Journal of Geophysical Research*, *114*, A08305. https://doi.org/10.1029/2008JA014001

Thomson, N. R., Rodger, C. J., & Clilverd, M. A. (2005). Large solar flares and the ionospheric D-region enhancements. *Journal of Geophysical Research*, *110*, A06306. https://doi.org/10.1029/2005JA011008

Thomson, N. R., Rodger, C. J., & Clilverd, M. A. (2011). Daytime D region parameters from long path VLF phase and amplitude. *Journal of Geophysical Research*, *116*, A11305. https://doi.org/10.1029/2011JA016910

Thorne, R. M., Church, S. R., & Gorney, D. J. (1979). On the origin of plasmaspheric hiss: The importance of wave propagation and the plasmapause. *Journal of Geophysical Research*, *84*(A9), 5241–5247. https://doi.org/10.1029/JA084iA09p05241

Thorne, R. M., & Kennel, C. F. (1971). Relativistic electron precipitation during magnetic storm main phase. *Journal of Geophysical Research*, *76*(19), 4446–4453. https://doi.org/10.1029/JA076i019p04446

Thorne, R. M., Li, W., Ni, B., Ma, Q., Bortnik, J., Chen, L., & Kletzing, C. A. (2013). Rapid local acceleration of relativistic radiation-belt electrons by magnetospheric chorus. *Nature*, *504*(7480), 411–414. https://doi.org/10.1038/nature12889

Thorne, R. M., O'Brien, T. P., Shprits, Y. Y., Summers, D., & Horne, R. B. (2005). Timescale for MeV electron microburst loss during geomagnetic storms. *Journal of Geophysical Research*, *110*, A09202. https://doi.org/10.1029/2004JA010882

Thorne, R. M., Smith, E. J., Burton, R. K., & Holzer, R. E. (1973). Plasmaspheric hiss. *Journal of Geophysical Research*, *78*(10), 1581–1596. https://doi.org/10.1029/JA078i010p01581

Tsurutani, B. T., Hajra, R., Tanimori, T., Takada, A., Remya, B., Mannucci, A. J., & Echer, E. (2016). Heliospheric plasma sheet (HPS) impingement onto the magnetosphere as a cause of relativistic electron dropouts (REDs) via coherent EMIC wave scattering with possible consequences for climate change mechanisms. *Journal of Geophysical Research: Space Physics*, *121*, 10,130–10,156. https://doi.org/10.1002/2016JA022499

Tsurutani, B. T., & Smith, E. J. (1974). Postmidnight chorus: A substorm phenomenon. *Journal of Geophysical Research*, *79*(1), 118–127. https://doi.org/10.1029/JA079i001p00118

Turner, D. L., Angelopoulos, V., Li, W., Bortnik, J., Ni, B., Ma, Q., et al. (2014). Competing source and loss mechanisms due to wave–particle interactions in Earth's outer radiation belt during the 30 September to 3 October 2012 geomagnetic storm. *Journal of Geophysical Research: Space Physics*, *119*, 1960–1979. https://doi.org/10.1002/2014JA019770

Ukhorskiy, A. Y., Anderson, B. J., Brandt, P. C., & Tsyganenko, N. A. (2006). Storm time evolution of the outer radiation belt: Transport and losses. *Journal of Geophysical Research*, *111*, A11S03. https://doi.org/10.1029/2006JA011690

Ukhorskiy, A. Y., Shprits, Y. Y., Anderson, B. J., Takahashi, K., & Thorne, R. M. (2010). Rapid scattering of radiation belt electrons by storm–time EMIC waves. *Geophysical Research Letters*, *37*, L09101. https://doi.org/10.1029/2010GL042906

Voss, H. D., Walt, M., Imhof, W. L., Mobilia, J., & Inan, U. S. (1998). Satellite observations of lightning-induced electron precipitation. *Journal of Geophysical Research*, *103*(A6), 11,725–11,744. https://doi.org/10.1029/97JA02878

Wait, J. R., and Spies, K. P. (1964). Characteristics of the Earth-ionosphere waveguide for VLF radio waves (No. 300). US Dept. of Commerce, National Bureau of Standards: for sale by the Supt. of Doc., US Govt. Print. Off

West, H. I., Buck, R. M., & Walton, J. R. (1973). Electron pitch angle distributions throughout the magnetosphere as observed on Ogo 5. *Journal of Geophysical Research*, *78*(7), 1064–1081. https://doi.org/10.1029/JA078i007p01064

Wu, C. C., Liou, K., Lepping, R. P., Hutting, L., Plunkett, S., Howard, R. A., & Socker, D. (2016). The first super geomagnetic storm of solar cycle 24: "The St. Patrick's day event (17 March 2015)". *Earth, Planets and Space*, *68*, 151. https://doi.org/10.1186/s40623-016-0525-y

Xiang, Z., Tu, W., Li, X., Ni, B., Morley, S. K., & Baker, D. N. (2017). Understanding the mechanisms of radiation belt dropouts observed by Van Allen Probes. *Journal of Geophysical Research: Space Physics*, *122*, 9858–9879. https://doi.org/10.1002/2017JA024487

Yando, K., Millan, R. M., Green, J. C., & Evans, D. S. (2011). A Monte Carlo simulation of the NOAA POES Medium Energy Proton and Electron Detector instrument. *Journal of Geophysical Research*, *116*, A10231. https://doi.org/10.1029/2011JA016671

Yu, Y., Koller, J., & Morley, S. K. (2013). Quantifying the effect of magnetopause shadowing on electron radiation belt dropouts. *Annales de Geophysique*, *31*, 1929–1939. https://doi.org/10.5194/angeo-31-1929-2013

Zhang, K., Li, X., Schiller, Q., Gerhardt, D., Zhao, H., & Millan, R. (2017). Detailed characteristics of radiation belt electrons revealed by CSSWE/REPTile measurements: Geomagnetic activity response and precipitation observation. *Journal of Geophysical Research: Space Physics*, *122*, 8434–8445. https://doi.org/10.1002/2017JA024309

Zhang, X. J., Li, W., Thorne, R. M., Angelopoulos, V., Ma, Q., Li, J., & Reeves, G. D. (2016). Physical mechanism causing rapid changes in ultrarelativistic electron pitch angle distributions right after a shock arrival: Evaluation of an electron dropout event. *Journal of Geophysical Research: Space Physics*, *121*, 8300–8316. https://doi.org/10.1002/2016JA022517